A Time-Frequency Deep Learning Classification Model for Metal Oxide Coated Particles

Muhammad Nabeel Tahir
Department of Electrical
Engineering
Rutgers the State University of
New Jersey
Piscataway, USA
nabeel.tahir@rutgers.edu

Brandon K Ashley
Department of Biomedical
Engineering
Rutgers the State University of
New Jersey
Piscataway, USA
brandon.ashley@rutgers.edu

Jianye Sui
Department of Electrical
Engineering
Rutgers the State University of
New Jersey
Piscataway, USA
js2001@scarletmail.rutgers.edu

Mehdi Javanmard
Department of Electrical
Engineering
Rutgers the State University of
New Jersey
Piscataway, USA
mehdi.javanmard @rutgers.edu

Umer Hassan*
Department of Electrical
Engineering
Rutgers the State University of
New Jersey
Piscataway, USA
umer.hassan@rutgers.edu

Abstract— **This study uses time-frequency transformed data and deep learning (DL) models to identify the groups of metal oxide nano-coated micro-particles using an impedance cytometer. The nano-coated bioparticles generate distinct electrical signals in a multifrequency electric field and can be used in biosensing applications. The current machine learning-enabled sensing modalities are unable to accurately differentiate different bioparticles as the feature selection and feature engineering techniques are ineffective in selecting useful and informative features. Here, we use Wigner-Vile Distribution to transform the time series data into the time-frequency domain and employ three deep learning models to evaluate the ability of time-frequency transformed data to accurately represent the most important features. A classification accuracy of 75% for (10nm and 30nm) coated particles was achieved on the simplest DL model. This combination of time-frequency representation and the DL model will be sufficient to differentiate bioparticles by acting as an alternative to other ML-based techniques.**

Keywords— Deep Learning, multiplexing, microfluidic, impedance cytometer

I. INTRODUCTION

Modern disease diagnostic methodologies use bioparticle quantification and biomarker detection as a primary tool to investigate the state and the progression of the disease. Tracking the number of bioparticles with certain biomarkers expressed on the surface can help clinicians to better diagnose and provide treatment. For example, human leukocyte counting can help in the diagnosis and prognosis of many diseases [1]–[4]. Various advanced techniques are available to quantify the micro-nano bioparticle. These techniques vary in their ability to process the biological samples, sensing techniques, and biomarker detection range. In general, cell cytometers are classified into two major categories manual and automated cell quantification. In the manual cell counting process, e.g.,

hemocytometer, a trained lab technician prepares a sample slide and manually counts the cells by using complex imaging tools such as a fluorescence microscope. The overall process is tedious, time-consuming, and subject to human processing errors. A fluorescent flow cell cytometry is one of the advanced techniques and can be used to quantify the fluorescently stained cells for up to 18 receptors expressed on the cell with high precision [5]–[7]. The equipment cost, operational cost, and the time required to process the complex data increase exponentially when the detection ability of more receptors is introduced in the fluorescent flow cytometer [8]–[11]. Static microscopic techniques try to address these issues. These techniques include high-resolution microscopy [12], [13], optical microscopy [14], [15], and smartphone microscopy (SFM) [16]–[18]. Images captured using these microscopic techniques were processed using either machine learning [19] or classical image processing tools [18], [20], [21]. All of these microscopic techniques highly rely on the excitation coefficients of the fluorophores, the quality of image-capturing platforms, and high-resolution image-processing resources. Which further increases the operational cost of the entire system and makes them impractical for commercial applications.

The impedance cytometry tries to address the challenges in the above-mentioned approaches. A bioparticle when passed through a micro/nanofluidic channel generates an electrical signal [22], [23]. The information encoded in the electrical signal is then used to isolate the population of the bioparticles [24]. New research studies tried to increase the diagnostic ability of impedance cytometers by using nano-coated bioparticles [23]. These coated particles when passed through a multifrequency electric field generate a unique signal that introduces the multiplexed biosensing ability in an impedance flow cytometer. The multiplexing ability increases the measuring range of the cytometer up to 20 analytes [25]. To

*corresponding author

address the strenuous data processing when more measurements are decorrelated in multiplexing techniques, machine learning techniques [26], [27] have been adopted to automate the analyte classification. These techniques highly rely on feature engineering and appropriate feature selection and are subject to human processing errors. Selecting the wrong set of features can highly bias the classification ability of the model and result in inaccurate predictions. Hence, creates a need to design a new algorithm where feature selection is automated and is independent of selection bias.

Herein, a time-frequency representation (Wigner-Vile Distribution) WVD has been employed to transform the multi-frequency electrical signal assuming spectral content in the signal will aid in identifying the bioparticle. The technique highlights the spatiotemporal features in the electrical signal and represents them in the spatial domain. A custom-designed convolutional neural network (CNN) model and two advanced deep learning models (ResNet50 and VGG16) were trained on
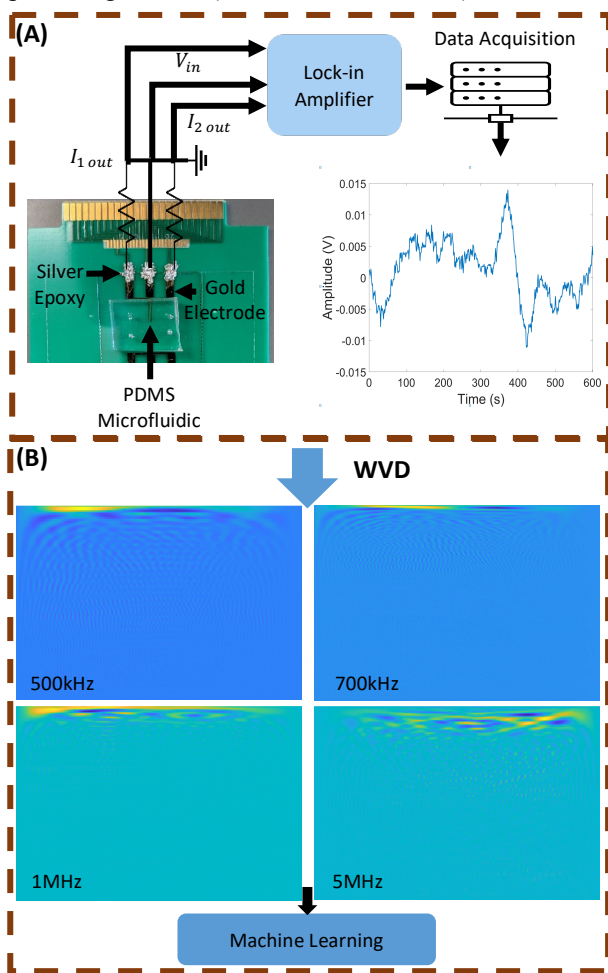

Figure 1: Data collection and algorithm flow chart. (A) Experimental setup showing the microfluidic device, multifrequency lock-in amplifier, data acquisition unit, and generated electrical signal. (B) A time-frequency representation of the collected electrical signal.

the image data generated by the WVD. The diagnostic ability and classification performance of all the models are compared.

II. METHODS AND MATERIALS

A. Experimental setup and data collection

The experimental setup and data collection protocol builds upon the process discussed in the study [26]. The data collection device consists of PCB containing gold-plated electrodes, a PDMS-based microfluidic device, a multi-frequency lock-in amplifier, and a data acquisition unit as shown the Fig. 1(A). First, two different nano-coated particles (NCPs) were fabricated by depositing 10nm and 30nm layers of Al_2O_2 on the 3µm polystyrene microparticles acting as the core particles respectively. For each NCP a stock solution that was diluted in 1X PBS at a ratio of 1:20 dilution was prepared. The prepared solution was pumped into PDMS microfluidic channel using a syringe pump at a flow rate of 15µL/min. An input signal of 8V was applied to the electrodes using a lock-in amplifier containing four different frequency components (500kHz, 700kHz, 1MHz, and 5MHz). The current output signals from the two electrodes were passed to a differential amplifier and converted to a single respective voltage signal. The final signal was demodulated in the lock-in amplifier and was sampled with a PCIe-6361 data acquisition unit at a sampling rate of 250kHz. To improve the quality and suppress the low-frequency components in the sampled signal, a 4th order high pass Butterworth filter was applied with cutoff frequency at 20Hz. To further reduce the noise signature a 4th order low pass Butterworth filter with a cutoff frequency at 100kHz, and a 1st order band-stop filter with cutoff frequencies at 60 and 120Hz was applied.

B. Time-frequency distribuiton

In classical signal processing, Fourier Transform (FT) is a fundamental technique to decompose a signal into its harmonic components, which helps to identify the spectral content in the signal. But if the signal contains evolving frequency components the FT fails to capture the information. A time-frequency distribution (TFD) helps in capturing the change in frequency content over time in a time series data with high time and frequency resolution. This study uses Wigner-Vile Distribution (WVD) as the TFD technique. Instead of using the actual signal, WVD transforms a form of autocorrelation term of the signal called ambiguity function. The Wigner-Vile Distribution $WV D_x(t,\omega)$ for a signal $s(t)$ is defined as:

$$W_s(t, \omega) = \int_{-\infty}^{\infty} s(t + \frac{\tau}{2})s^*(t - \frac{\tau}{2})e^{j\omega\tau}\,d\tau \qquad (1)$$

The above distribution (1) was applied to each signal pulse generated for a particle passing through the microfluidic channel. The transformed signals generated for all four input frequency signals (500kHz, 700kHz, 1MHz, and 5MHz) were concatenated and saved as a single image. Thus each signal pulse resulted in a single image for nano-coated particles 10*nm* or 30*nm* as shown in Fig. 1(B).

C. Deep convolutional neural networks

Assuming that the data generated in II-B contains the spectral density changes in the time domain, and now has the spatial representation, more complex and useful features can be extracted from the data. Which later can be used to train an advanced machine learning algorithm more specifically deep neural networks. Deep convolutional neural networks (DCNNs) are the most common machine learning techniques available that could be employed to identify the patterns and classify the images. In this study, a custom-designed CNN model was trained and evaluated along with state-of-the-art deep convolutional neural networks (ResNet50 and VGG16) by applying transfer learning.

1) Dataset Preparation: The application of a TFD technique as discussed in II-B resulted in the image data that
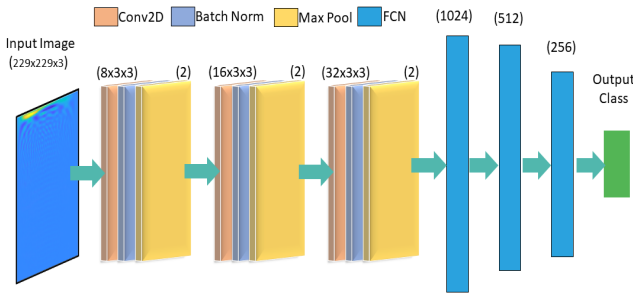

Figure 2: Architectural diagram of the proposed custom CNN model to classify the time-frequency transformed particle images.

was annotated into two classes (10nm and 30nm). The dataset was then divided into the train, test, and validation sets with ratios of 70%, 20%, and 10% respectively. All the CNN models were trained on the data with 5000 training and 2500 in test and validation instances for each class.

2) Proposed convolutional neural network: In an artificial neural network (ANN), when an input is passed from one layer to another it is multiplied by the weight of the neural link. The result for all the input neurons once multiplied with the weights is added along with an additional term called bias. The final output is called the input of the second neuron layer and then a nonlinearity is added to the output of the second layer by applying an activation function. This process of passing the input signal from all the layers of a neural network and computing the final value is called forward propagation. The output layer of the neural network provides the probabilities of each class variable and the class with the highest probability is considered the final prediction of the neural network. For each class variable, an error function is evaluated and the information is passed from output to input layers through a process called backpropagation. During this process, the weights of all the neural links are updated which is also called the training of the neural network.

A convolutional neural network model containing convolution, batch normalization, max pooling, and dense layers was implemented. The training process of a CNN model varies from a traditional ANN model in the sense that instead of traditional matrix multiplication another mathematical operation called convolution is used. In forward propagation a kernel of fixed size is convolved with the input image and the outcome is passed to the other layer where nonlinearity is applied. And in the backpropagation step instead of learning the weights of each neural link (one image pixel to the other), the weights of the kernel are updated. The output of the convolution with the kernel helps in learning the specialized features and patterns in the input image. Changing the size and number of kernels applied to a single image aid in learning more complex and advanced features, which later can be used by classification layers to differentiate the classes.

An input image of the size **229×229×3** was fed into the first 2D convolution layer that applies 8 kernels to the image each of the size **3×3**. The output is then passed through a batch normalization layer which re-centers and re-scales the data, a ReLU activation layer, and a max pooling layer with a pool size of 2. The max pooling layer preserves the important features in the feature map by applying a max filter in a non-overlapping area or pool of selected pixels. The process reduces the dimensionality of the matrix and generates an output with dimensions of **149×149×8**. The output is passed through the second and third convolution layers each applying total of 16 and 32 filters respectively, along with the batch normalization, activation, and max pooling layers. Which results in an output of size **74×74×32**. The output of this layer is flattened and then passed through three dense layers of sizes **1024**, **512**, and **256** respectively. The final output is passed through the classification layer that generates the class probabilities. Fig. 2 shows the architectural diagram of the custom CNN model explaining the size and filters in each layer.

3) Transfer learning with ResNet50 and VGG16: A transfer learning technique is employed to draw a comparison of our proposed CNN model with more advanced DCNN models. Two of the most widely used and efficient state-of-the-art DCNN models VGG16 and ResNet50 were used in the transfer learning. VGG16 is a deep convolutional neural network that is 16 layers deep. It contains **13** convolution layers and **3** dense layers and an output or classification layer. ResNet50 is **50** layers deep convolutional neural network. It contains four stages of residual blocks, each containing multiple convolution layers, a dense layer, and an output layer. Both DCNN models are pre-trained on one million images from the ImageNet dataset containing **1000** categories. In transfer learning, we replace the fully connected and classification layers in both the DCNN models with three new fully connected layers of size **512**, **256**, and **128** neurons and a classification layer customized to our problem under consideration. The newly added layers in ResNet50 and VGG16 were trained while the weights of CNN layers were kept intact. Thus helping in reducing the overall training time required to train a deep neural network and benefiting from the information gained while the models were trained on other datasets.

4) Hyperparameters and training environment: The training and learning of a neural network are governed by the choice of the loss function, suitable optimization algorithm, and
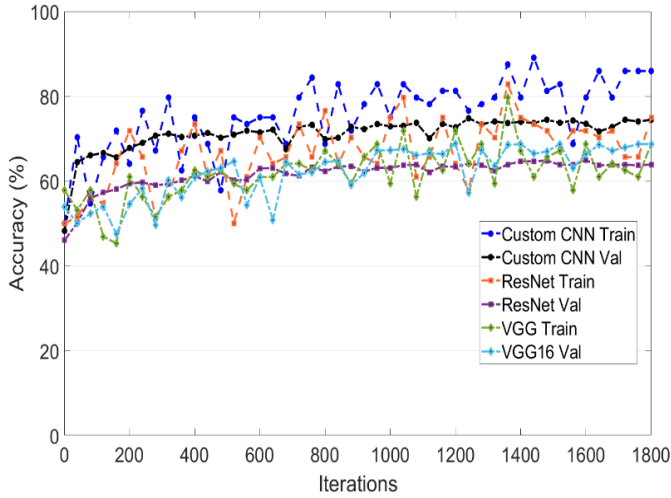
Figure 3: Plots comparing the training and validation accuracy of custom CNN, ResNet50, and VGG16 models.

appropriate selection of hyperparameters (e.g. learning rate). The stochastic gradient descent was used as an optimization classification layer. A batch size of 64 was used for all the models with a validation frequency of 40. Both VGG16 and ResNet50 have been trained for **20** epochs with a learning rate
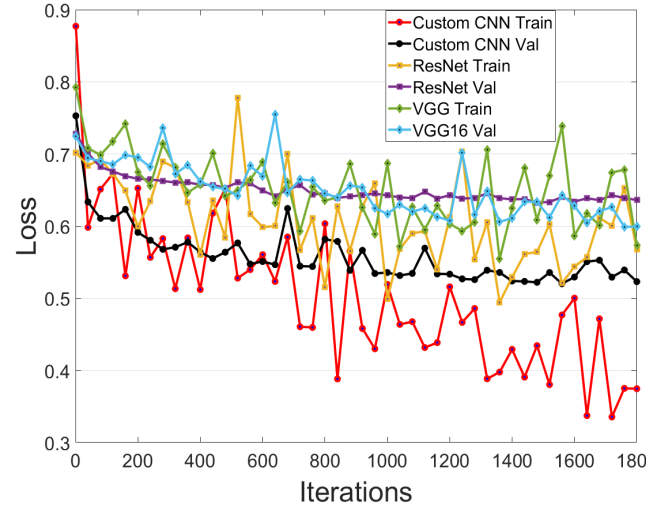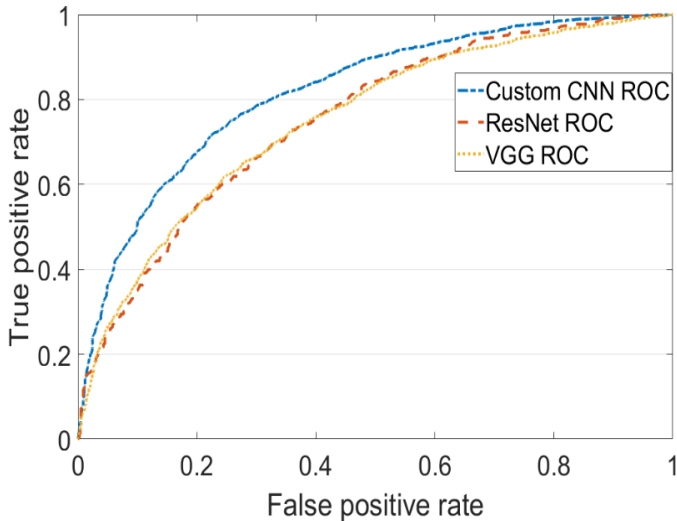

Figure 4: Plots comparing the receiver operating curves (ROCs) of the custom CNN, ResNet50, and VGG16 models.

of **0.001**, while the custom CNN model was trained for **10** epochs with a learning rate of **0.001**. All the models were trained in a system (Core i9, 10th Gen, 32GB RAM) using algorithm, along with the cross-entropy loss function for the MATLAB as the development environment.

III. RESULTS AND DISCUSSION

A. Proposed CNN evaluation

While training the custom CNN model the plots of training accuracy and validation accuracy were generated. The frequency of the validation step was kept at 40 to minimize the total training time. Fig. 3 shows the training and validation

Figure 5: Plots comparing the training and validation loss of custom CNN, ResNet50, and VGG16 models.

accuracies plotted in each epoch. A validation accuracy of 75.34% was achieved with only three convolutional and dense layers. To further evaluate the performance of the trained model receiver operating characteristic curve (ROC) of the model was generated on unseen test data as shown in Fig. 4. ROC curve demonstrates the diagnostic ability of the binary classifier and evaluates the model's selectivity and specificity towards group identification. An area under the curve (AUC) of 0.81 as shown in table 1 was achieved on the test data. This demonstrates that the simplest deep-learning model can be used to classify the time-frequency distributed electrical signal when passed through a frequency-simulated microfluidic impedance cytometer. Apart from the training accuracies, the cross entropy loss function was evaluated at each training iteration, the results of which are plotted in Fig. 5. Figure 5 shows the loss plots of the training and validation for the custom CNN model. Starting with the training loss of ~0.9 and validation loss of 0.75 at the end of the training cycle the training and validation losses are reduced to ~0.5 and ~0.4 respectively. It can be observed from figure 5 that the training loss follows a decreasing trend as the number of training iterations increases while the validation loss decreases at a very slow rate. This could be a sign of overfitting the data as the validation loss is higher than the training loss and follows steady variations. To **remedy the issue a dataset containing less variance for each** class variable will be generated. Hence, increasing the size of the dataset the generalizability of the model can be achieved. Moreover, results

B. ResNet50 and VGG16 evaluation

Similar to custom CNN the training and validation accuracy plots were generated for both ResNet50 and VGG16 for each epoch. A validation accuracy of 70% for ResNet50 and 68.7% for VGG16 was observed as summarized in table 1 and the plots generated are shown in Fig. 3. On the test data, the trained ResNet50 and VGG16 generated the AUCs of 0.76 and 0.75 respectively, and Fig 4 shows the ROC curves for both models.

Fig. 5 also shows the training and validation losses for both ResNet and VGG16 plotted against the number of training iterations. The ResNet50's validation loss reduces as the training progresses and achieves a steady state condition somewhere ~0.65, while the training loss keeps on oscillating around the validation loss. The trend suggests that the ResNet50 is not completely trained and requires more training iterations. VGG16 underperforms the other reported CNN models. Although the validation loss of VGG16 is slightly lower than the ResNet50 at the end of the training cycle. Since the transfer learning approach was adopted for both deep neural networks with the time-frequency data. But the training loss contains significant random variations due to the inability of VGG16 to fully capture the information in the images. The underperformance of both algorithms can be justified by the fact that the ImageNet data that was previously used to train the models contained a set of features that are significantly different and alien to the features in the time-frequency representation of the time series data. Although the performance of the models is comparably less than the custom CNN model, it is particular enough to be considered that the models can be used in the classification of NCP-generated electrical signals. To fully utilize the potential of the VGG16 and ResNet50's deep convolutional layers the models will be trained on the data by applying various data augmentation techniques. Also, generating a new set of data with lower levels of variance will further improve the accuracies and differentiation ability of both algorithms.

Table 1: Accuracy

Model	Accuracy (%)	ROC AUC
Custom CNN	75.34	0.81
ResNet50	70.00	0.76
VGG16	68.70	0.75

IV. CONCLUSION

Three deep learning models were trained on time-frequency transformed data of multifrequency signals generated by the impedance cytometer. An accuracy of 75.34% was achieved with a custom-designed CNN model outperforming the state-of-the-art deep learning models. These results establish a concrete ground for using time-frequency distribution as a potential feature space alternative. Moreover, the results are aligned with the other ML-based approaches in an agreeable error range. This further strengthens the case for TFD-based feature selection techniques to be used as inputs for DL models. In future work, generating data at multiple frequencies of the lock-in amplifier and using different TFD techniques (e.g. Wavelet) which might introduce unique features that could be associated with a single class of nano-coated particles that can help in improving the performance and diagnostic efficiency of the models. Generating more data and using complex CNN layers in the custom neural network can also improve the accuracy of the model is a direction worth exploring.

V. ACKNOWLEDGEMENTS

VI. REFERENCES

[1] R. H. Grimm and J. D. Neaton, "Prognostic Importance of the White Blood Cell Count for Coronary, Cancer, and All-Cause Mortality".

[2] G. Giugliano, G. Brevetti, S. Lanero, V. Schiano, E. Laurenzano, and M. Chiariello, "Leukocyte count in peripheral arterial disease: A simple, reliable, inexpensive approach to cardiovascular risk prediction," *Atherosclerosis*, vol. 210, no. 1, pp. 288–293, May 2010, doi: 10.1016/j.atherosclerosis.2009.11.009.

[3] J. O. Rodríguez *et al.*, "Predictions of CD4 lymphocytes' count in HIV patients from complete blood count," *BMC Med. Phys.*, vol. 13, no. 1, p. 3, Dec. 2013, doi: 10.1186/1756-6649-13-3.

[4] G. S. Philip and R. Hewitt, "Early Diagnosis of Neonatal Sepsis".

[5] E. S. Graham, C. E. Angel, L. E. Schwarcz, P. R. Dunbar, and M. Glass, "Detailed Characterisation of CB2 Receptor Protein Expression in Peripheral Blood Immune Cells from Healthy Human Volunteers Using Flow Cytometry," *Int. J. Immunopathol. Pharmacol.*, vol. 23, no. 1, pp. 25–34, Jan. 2010, doi: 10.1177/039463201002300103.

[6] H. Jin, M. Aziz, Y. Ode, and P. Wang, "CIRP Induces Neutrophil Reverse Transendothelial Migration in Sepsis," *Shock*, vol. 51, no. 5, pp. 548–556, May 2019, doi: 10.1097/SHK.0000000000001257.

[7] D. Saygin *et al.*, "Relative quantification of beta-adrenergic receptor in peripheral blood cells using flow cytometry," *Cytometry A*, vol. 93, no. 5, pp. 563–570, May 2018, doi: 10.1002/cyto.a.23358.

[8] L. M. Park, J. Lannigan, and M. C. Jaimes, "OMIP-069 : Forty-Color Full Spectrum Flow Cytometry Panel for Deep Immunophenotyping of Major Cell Subsets in Human Peripheral Blood," *Cytometry A*, vol. 97, no. 10, pp. 1044–1051, Oct. 2020, doi: 10.1002/cyto.a.24213.

[9] T. Maetzig *et al.*, "A Lentiviral Fluorescent Genetic Barcoding System for Flow Cytometry-Based Multiplex Tracking," *Mol. Ther.*, vol. 25, no. 3, pp. 606–620, Mar. 2017, doi: 10.1016/j.ymthe.2016.12.005.

[10] V. N. Umlauf, S. Dreschers, and T. W. Orlikowsky, "Flow Cytometry in the Detection of Neonatal Sepsis," *Int. J. Pediatr.*, vol. 2013, pp. 1–6, 2013, doi: 10.1155/2013/763191.

[11] B. K. Ashley and U. Hassan, "POINT-OF-CRITICAL-CARE diagnostics for sepsis enabled by multiplexed MICRO AND NANO sensing technologies," *WIREs Nanomedicine Nanobiotechnology*, vol. 13, no. 5, Sep. 2021, doi: 10.1002/wnan.1701.

[12] B. Huang, H. Babcock, and X. Zhuang, "Breaking the Diffraction Barrier: Super-Resolution Imaging of Cells," *Cell*, vol. 143, no. 7, pp. 1047–1058, Dec. 2010, doi: 10.1016/j.cell.2010.12.002.

[13] B. Yang *et al.*, "Sub-nanometre resolution in single-molecule photoluminescence imaging," *Nat. Photonics*, vol. 14, no. 11, pp. 693–699, Nov. 2020, doi: 10.1038/s41566-020-0677-y.

[14] K. Frischwasser, K. Cohen, J. Kher-Alden, S. Dolev, S. Tsesses, and G. Bartal, "Real-time sub-wavelength imaging of surface waves with nonlinear near-field optical microscopy," *Nat. Photonics*, vol. 15, no. 6, pp. 442–448, Jun. 2021, doi: 10.1038/s41566-021-00782-2.

[15] E. Betzig and R. J. Chichester, "Single Molecules Observed by Near-Field Scanning Optical Microscopy," *Science*, vol. 262, no. 5138, pp. 1422–1425, Nov. 1993, doi: 10.1126/science.262.5138.1422.

[16] K. Yuan *et al.*, "Smartphone-based hand-held polarized light microscope for on-site pharmaceutical crystallinity characterization," *Anal. Bioanal. Chem.*, Feb. 2023, doi: 10.1007/s00216-023-04582-1.

[17] K. Kim and W. G. Lee, "Portable, Automated and Deep-Learning-Enabled Microscopy for Smartphone-Tethered Optical Platform Towards Remote Homecare Diagnostics: A Review," *Small Methods*, vol. 7, no. 1, p. 2200979, Jan. 2023, doi: 10.1002/smtd.202200979.

[18] M. A. Sami, M. Tayyab, and U. Hassan, "Excitation modalities for enhanced micro and nanoparticle imaging in a smartphone coupled 3D printed fluorescent microscope," *Lab. Chip*, vol. 22, no. 19, pp. 3755–3769, 2022, doi: 10.1039/D2LC00589A.

[19] H. Govindaraju, M. A. Sami, and U. Hassan, "Particle Quantification from a Smartphone-based Biosensor using Deep Convolutional Neural Network for Clinical Diagnosis," in *2022 IEEE Healthcare Innovations and Point of Care Technologies (HI-POCT)*, Houston, TX, USA, Mar. 2022, pp. 113–116. doi: 10.1109/HI-POCT54491.2022.9744062.

[20] M. Krogsbaek, N. Y. Larsen, A. M. Landau, C. Sanchez, and J. R. Nyengaard, "Spatial quantification of single cell mRNA and ligand binding of the kappa opioid receptor in the rat hypothalamus," *J. Chem. Neuroanat.*, vol. 127, p. 102205, Jan. 2023, doi: 10.1016/j.jchemneu.2022.102205.

[21] P. Danaher *et al.*, "Advances in mixed cell deconvolution enable quantification of cell types in spatial transcriptomic data," *Nat. Commun.*, vol. 13, no. 1, p. 385, Jan. 2022, doi: 10.1038/s41467-022-28020-5.

[22] O. A. Saleh and L. L. Sohn, "Direct detection of antibody–antigen binding using an on-chip artificial pore," *Proc. Natl. Acad. Sci.*, vol. 100, no. 3, pp. 820–824, Feb. 2003, doi: 10.1073/pnas.0337563100.

[23] J. Sui, N. Gandotra, P. Xie, Z. Lin, C. Scharfe, and M. Javanmard, "Multi-frequency impedance sensing for detection and sizing of DNA fragments," *Sci. Rep.*, vol. 11, no. 1, p. 6490, Mar. 2021, doi: 10.1038/s41598-021-85755-9.

[24] U. Hassan *et al.*, "A point-of-care microfluidic biochip for quantification of CD64 expression from whole blood for sepsis stratification," *Nat. Commun.*, vol. 8, no. 1, p. 15949, Jul. 2017, doi: 10.1038/ncomms15949.

[25] B. Lam *et al.*, "Solution-based circuits enable rapid and multiplexed pathogen detection," *Nat. Commun.*, vol. 4, no. 1, p. 2001, Jun. 2013, doi: 10.1038/ncomms3001.

[26] B. K. Ashley, J. Sui, M. Javanmard, and U. Hassan, "Aluminum Oxide-Coated Particle Differentiation Employing Supervised Machine Learning and Impedance Cytometry," in *2022 IEEE 17th International Conference on Nano/Micro Engineered and Molecular Systems (NEMS)*, Taoyuan, Taiwan, Apr. 2022, pp. 211–216. doi: 10.1109/NEMS54180.2022.9791160.

[27] C. Honrado, J. S. McGrath, R. Reale, P. Bisegna, N. S. Swami, and F. Caselli, "A neural network approach for real-time particle/cell characterization in microfluidic impedance cytometry," *Anal. Bioanal. Chem.*, vol. 412, no. 16, pp. 3835–3845, Jun. 2020, doi: 10.1007/s00216-020-02497-9.